Effect of high oxygen deficiency in nano-confined bismuth sesquioxide

IOP Publishing Journal Title
Journal **XX** (XXXX) XXXXXX https://doi.org/XXXX/XXXX

Effect of high oxygen deficiency in nano-confined bismuth sesquioxide

Simone Sanna[1,2], Elisabetta Maria Firodaliso[3], Takeshi Kasama[3] , Ivano E. Castelli[1] and Vincenzo Esposito[1*]

[1] Department of Energy Conversion and Storage, Technical University of Denmark, DK-2800 Kongens Lyngby, Denmark
[2] DICII, Università di Roma Tor Vergata, Via del Politecnico 1, I-00133 Roma, Italy
[3] DTU Nanolab - National Centre for Nano Fabrication and Characterization, Technical University of Denmark, DK-2800 Kongens Lyngby, Denmark
E-mail: vies@dtu.dk (VE)

Received xxxxxx
Accepted for publication xxxxxx
Published xxxxxx

Abstract

Bismuth sesquioxide in its cubic form, i.e. δ-Bi_2O_3, is the fastest oxygen ionic conductor known with important applications in energy technologies. However, the material is unstable as it undergoes to high-density polymorphic transitions and degradation. In this work, we show that δ-Bi_2O_3 can be stabilized both at high and low temperatures (T < 775 °C) under low oxygen partial pressure (pO_2 < 10^{-5} atm), where the material is nanostructured in multi-layered thin film coherent heterostructures with yttrium stabilized zirconia (YSZ). DFT calculation confirms such a form of metastability, also showing that high oxygen defect concentration favors the cubic phase. Moreover, high oxygen deficiency in the nanoionics leads to an unexpected "two-regime" conductivity with high values (σ > 1 S cm^{-1} at 600 °C) at high pO_2 and lower ionic conductivity (σ ~ 0.1 S cm^{-1} at 600 °C) at low pO_2. Ionic conductivity at low pO_2 occurs with high activation energy (Ea > 1.5 eV), suggesting thus a drastic decrease in mobility for high concentration of defects.

Keywords: Bi_2O_3, YSZ, Heterostructure, thin films, nanoionics

1. Introduction

Defective metal oxides (MeOx) that can transport oxygen at high and intermediate temperatures are the core-components of key energy technologies such as fuel cells, electrolysers and sensors.[1,2] Besides such well-established applications, oxygen defective metal oxides are nowadays spreading in new fields, as in MEMS, ICT and Biomedical technologies.[3–5] Such an attainment relies on the high tunability of the defective chemistry of MeOx that can bring to the material wide range of properties either as the result of combination of functions or even by the arising of new properties that do not belong to constitutive components.[6] Among the different strategies of tuning, "nanostructuring" is probably the most promising one. This is the case of nanometric ionic conductive materials (nanoionics)[7] for miniaturized energy devices,[8] novel memory device concepts,[9] ionotronics [10] and minutuirized actutators.[11] These are made by reducing the shape to the ionic componet to the nanoscale and introducing interfaces between functional components.[6]

For the energy technologies, the search of high oxygen ionic conductivity has been the focus of intense investigation for the last decades, as it has been seen resolutive for reducing the operative temperature of solid oxide fuel cells and other energy devices.[12] Among the fast oxygen ionic conductors, bismuth sesquioxide in its cubic form, i.e. δ-Bi_2O_3, is the

fastest one.[13] However, the material is also chemically unstable with high density polymorphism: up to 5 phases can be found only in the Bi_2O_3 composition at high oxygen partial pressure (pO_2), e.g. in air and pure oxygen. Under low pO_2, the oxide gets reduced to the highly volatile metallic form.[13] On the other side, polymorphism can be retained by doping, i.e. cubic phase stabilization,[14] degradation under low pO_2 is difficult to prevent and it limits performances and applications.[15]

In our previous work, we have shown that nanostructuring of bismth oxide (both doped and undoped) in multilayered heterostrutures with other stable materials can lead to cubic stabilization at low pO_2 and unexpected electrical properties.[13,16] Nanostructuring can stabilize the bismuth oxide component beyond its thermodynamical stability, e.g. in highly reducing conditions (H_2) and at high temperatures.[13] We also found that the pure bismuth sesquioxide, with no doping, does not undergo to polymorphism in air at different temperatures and we observed that such a form of metastability depends on interface and lattice strain at the heterostrutures.[16] Particularly, in YSZ/δ-Bi_2O_3 heterostrutures with different numbers of interface and thicknesses, the YSZ component constrains the bismuth oxide in an overall large lattice that is able to host the oxygen defects in a larger extend than expected for the pure material.[16] Despite such results, the configuration of the defects in the heterostruture as well as their influence on the electrical properties at low pO_2 remains unexplored.

In the present paper, we analyse the thermochemical stability and electrical properties of YSZ/δ-Bi_2O_3 heterostrutures with thin layers of *ca.* 1, 2, 4 nm, giving a new insight on the structural factors that can influence ionic condutivity at the multilayer interface. We also characterize the the crystal structure of the multilayered material by using X-ray diffraction and electron microscopy. To clarify some theoretical aspects of the complex defective chemistry occurring at the nanoionic, we escort the experimental results with some *ab-initio* calculations, especially to define the effect of high defect concentration on the metastable cubic bismuth sesquioxide under low pO_2 and high temperatures.

2. Experimental

Thin films deposition

The heterostrucures were deposited by Pulsed Laser Depostion (PLD) tecnique onto $NdGaO_3$ single crystal (100) oriented. The alteranitive layers (YSZ/δ-Bi_2O_3) in the heterostructures were made by using a multi-target carousel in the vacuum chamber with the base pressure of 10^{-7} mbar. The ablation on the targets was made with A KrF excimer laser (Coherent Lambda Physik GmbH) having a wavelength of 248 nm and pulse duration of 25 ns. The laser energy was kept at 2J cm^{-2} at repetion rate of 2Hz. The substrate temperature during the deposition was at 600 °C with oxygen partial pressure about 10^{-2} mbar.

Thin films characterization

Structural analysis was carried out by X-ray Diffraction (XRD). θ-2θ scans and rocking curve analysis were performed using the Rigaku Smartlab diffractometer with X-ray beam monochromatized with a Cu (λ = 1.5418 Å) rotating anode.

Electrochemical impedance spectroscopy (EIS, Solartron 1260) measurements were perfomed in 400-750 °C temperature range in air, O_2 and H_2-N_2 atmosphere with fixed ratio of 3 vol. % hydrogen. Other mixutures were made by mixing N_2 and H_2-N_2 mixtures. For the electrochemical characterization, the frequency varied from 50Hz to 1MHz with 0.2 V alternating voltage signal.

Microstruture and thickness of the samples were measured by scanning electron microscopy (Zeiss SUPRA FEGSEM). Preparation of lamellas for scanning transmission electron microscopy (STEM) analysis was carried out by FIB (FEI Helios 600 Dual beam FIB/SEM) and STEM images were acquired at 300 kV by using a probe corrected TEM (FEI Analytical Titan), equipped with an energy dispersive X-ray (EDX) detector for chemical analysis.

Atomic-scale calculations

Atomic-scale calculations have been proved very successful in elucidating materials properties.[17] Here, we perform Density Functional Theory (DFT) calculations to explain the role of vacancies with respect to stability of polymorphic phases of Bi_2O_3 and diffusion barriers. All calculations have been performed using the GPAW code [19,20] and the Atomistic Simulation Environment (ASE).[20] All structure have been fully optimized until the forces where under 0.01 eV/Å, using PBEsol [21] as exchange-correlation functional, with a k-point density of at last 3 kpoints/Å. The Climbing Image Nudged Elastic Bands (CI-NEB) method [22,23] has been used to estimate the diffusion barriers for various concentrations and orderings of vacancies.

3. Results and discussion

Coherency and reduced thickness of the epitaxial fluorite structures in the multilayer are necessary conditions to obtain the chemical stabilization of highly defective metal

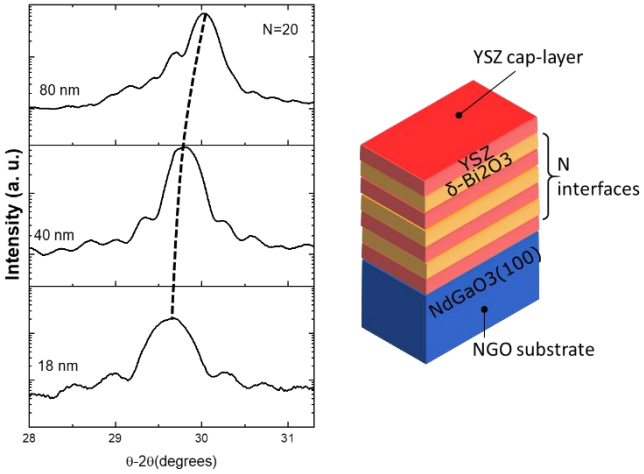

Figure 1: XRD diffraction patterns of NGO(100)/[YSZ/δ-Bi_2O_3/YSZ]$_{N=20}$ multilayers with and schematic representation of the architectures (right hand side).

oxides.[24–26] For bismuth sesquioxide, such conditions is achieved by depositing nanometric multilayer on single crystal substrates that present compatible lattice parameter with materials in the multilayer. This is the case of NGO (100) perovskite orthorhombic structure which is only 3.8% larger than YSZ (111), thus ensuring a coherent growth of bottom layer in the epitaxial film.[16] For the cubic δ-Bi_2O_3 over the cubic YSZ fluorite layers, the theortical lattice mismatch at room temperature is relatively low (5.14 Å for YSZ vs 5.66 Å for δ-Bi_2O_3), resulting in a coeherent heterostruture with a slightly compression of the δ-Bi_2O_3 layers.[16] In NGO (substrate)-YSZ-Bi_2O_3 sequence, the deposited multilayer structure results highly coherent and, depending on the number and thickness of the layers, an ordered and epitaxial heterostructure is arranged along the (111) orientation. **Figure 1** shows a schematic representation of the multilayer architecture and three examples of XRD results for NGO(100)/[YSZ/δ-Bi_2O_3/YSZ]$_{N=20}$ heterostructures, at a constant number of interfaces N = 20, with total thickness of 20, 40 and 80 nm. The diffraction patterns show the (111) reflection at 2θ between 29 and 30° with a typical sub-patterning around the main peaks for all the samples. Subpattern oscillations are a typical feature of the heterostructures multilayers.[25] Figure 1 also shows a slightly relaxation of the layers at from the thinner to thicker samples, with a nearly linear shift of the eaks to higher angles (see dashed line figure 1). Since the lattice parameter mismatch between the components is ca. 10%, i.e. of δ-Bi_2O_3 is 5.66 Å (lattice bulk) the lattice parameter of YSZ is 5.14 Å (lattice bulk), thin samples tend to be more strained with the increasing the number of the interfaces, especially in thin film samples (e.g. in the 18 nm sample in figure 1). Conversely, when layers became thicker (for example in the 40 to 80 nm samples, figure 1), the heterostruture tends to adapt to the lattice parameter of YSZ. These two effects also indicate that that the δ-Bi_2O_3 component is prone to strain more than YSZ in the multilayered arrangement [26]. The XRD patterns clearly also indicate a high coherency of the nanoscaled materials, confirming previous results on pure Bi_2O_3 and Er-stabilized bismuth sesquioxide.[13,16,27]

For the electrical properties, impedance spectroscopy characterization is carried out using in-plane electrodes configuration, especially to evaluate the effect of the layers´ thickness and interfaces on the total conductivity.[13] **Figure 2** show the Arrhenius and the Brower-like (conductivity as function of pO_2) plots of the total conductivity for the 40 and 80 nm thick samples in air and in low pO_2 conditions, *i.e.* in N_2 and in N_2-H_2 mixtures. Measurements are a collection of

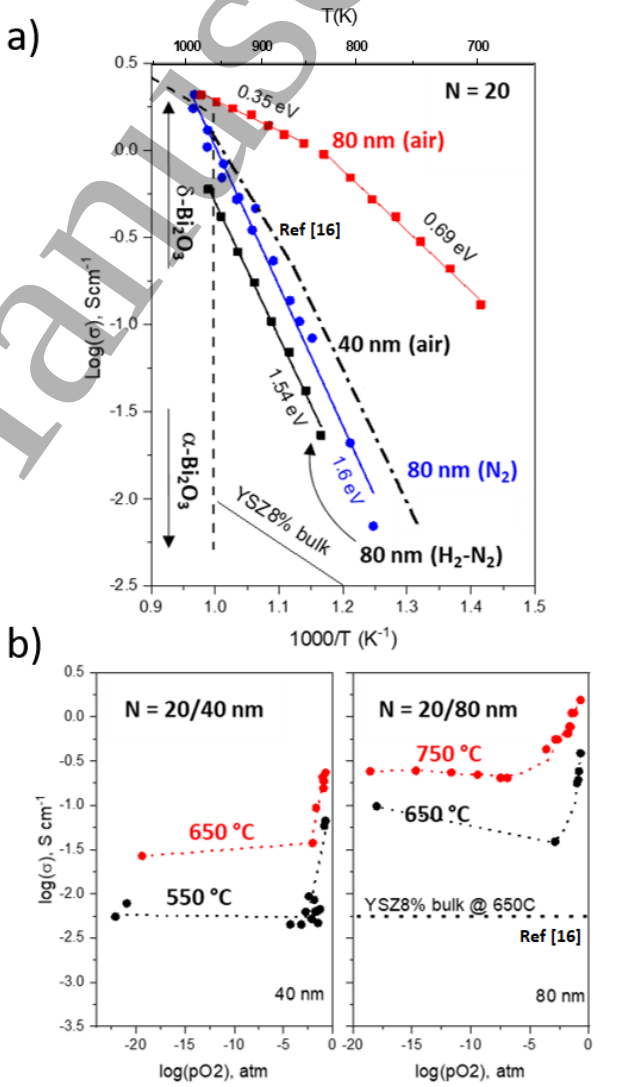

Figure 2: Conductivity of the NGO(100)/[YSZ/δ-Bi_2O_3/YSZ]$_{N=20}$multilayers as Arrhenius plot (a) of function of the temprature and pO_2, i.e. Brower-like (b), including references for bulk and other bismuth based heterostructures. [16]

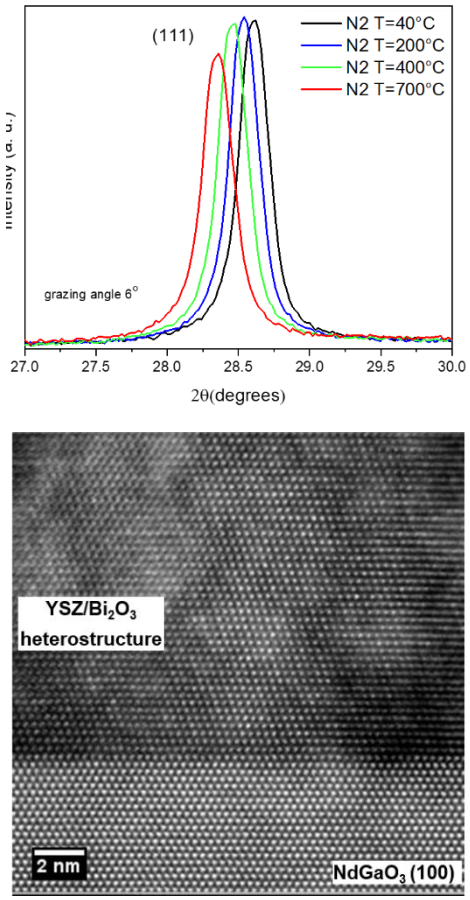

Figure 3: Top. Diffraction patterns of NGO(100)/[YSZ/δ-Bi_2O_3/YSZ]$_{N=20}$ multilayers of 40 nm during reduction under N_2 tretments. Bottom. HAADF-STEM image of the heterostructure showing epitaxial interfaces at the atomic level.

long (2-5 hours) isothermal measurements. Due to the high impedance, thin samples below 20 nm could not be measured consinstently and are not included. Figure 2 illustrates a collection of results on the conductivity as function of the temperature and pO_2. Data are compared with electrical coductivity of YSZ and Bi_2O_3 bulk materials and to similar N = 20 heterostructure reported in a previous publication.[16] In air, *i.e.* at pO_2 = 0.21 atm, we register a significant enhanchement of the condutivity with respect of both the costitutive materials (YSZ and δ-Bi_2O_3) and the 40 nm sample.[16] Results also show very large conductivity at low temperatures, i.e. 10^{-1} S cm^{-1} at 400 °C. Such high values of conductiviy are often measured in bismuth oxides based compounds, although they often appear rather unconsistent in the literature.[27–29] Interestingly, no change in conductivity is obsterved at T = 700 °C, as expected by the α– to δ–phase transition of Bi_2O_3 (dashed line Figure 2 top). However, a change in activation energy at *ca.* 600 °C is seen in the heterostruture, which, in the case of the 80 nm sample, changes from 0.35 eV at high temperatures to 0.69 eV at low temperatures. Changes in activation energy are generally observed in stabilized Bi_2O_3 by dopants [14] and not in YSZ. However, activation energies in the 80 nm heterostruture results lower than previously measured in bulk, thin film and in the 40 nm heterostruture (between 0.8-1.5 eV [16]). About the nature of the conductivity, both Bi_2O_3 and YSZ in air, are expected to be pure ionic conductors. However, due to the presence of several interfaces (N = 20) and the reduced size of the layers (*ca.* 2 nm each in the 40 nm sample and 4 nm for the 80 nm sample), formation of electronic defects and space charge regions is also possible.[6] Polarized species can especially gather at the YSZ/Bi_2O_3 interfaces and lead to lateral conductivity in the thin samples. However, this is not observed in the 40 nm sample, where conductivity is lower and the activation energies higher, in the range of 0.77 to 1.4 eV.[16] Electronic defects in ionic compounds as ZrO_2 and Bi_2O_3, such as small polarons, are unlikely formed under high pO_2, as they are induced either by a partial reduction of cations in the materials or by formation of other interstitial species in the lattice.[6] In both cases, the concentration of the charge carriers is stricly depended on the oxygen partial pressure at the enviroment.

To check the reactivity of the heterostructure toward the pO_2 we show in Figure 2 the Arrhenius plot carried out in N_2 and H_2-N_2 3 vol.%. For both the 80 nm and the 40 nm samples, the electrical properties are comparable in terms of conductivity and activation energies (only 80 nm sample shown in Figure 2 top). The conductivity decays especially at low temperatures, as result of a large increased in the activation energy, i.e. from 0.7 eV in air to *ca.* 1.5 eV in both N_2 and H_2-N_2. For the 40 nm sample in air and in N_2-H_2 resulted less affected by the change in pO_2 than the 80 nm samples. Such a

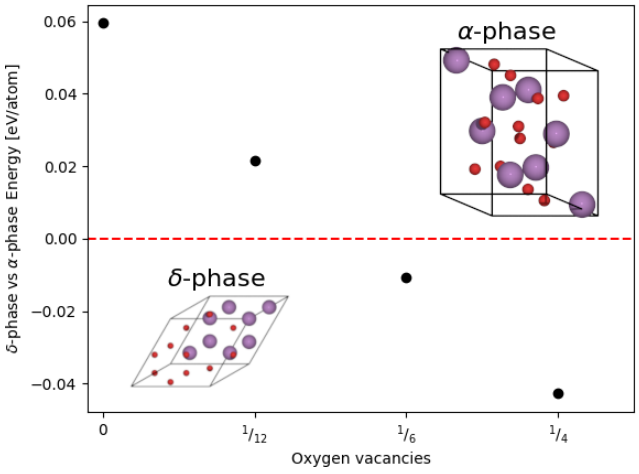

Figure 4: Energy difference between the delta and alpha phases of Bi_2O_3 as a function of the number of vacancies. An increase of the vacancy concentration is followed by a stabilization of the delta-phase versus the alpha-phase.

result is surprising as YSZ is expected to introduce n-type polarons at high temperature and very low pO_2 only, with an increase of total conductivity as addition of n-type conductivity to the pure ionic conducitivity.[30] Electrical properties of Bi_2O_3 under low pO_2 are unknown, as the material generally degrades below 10^{-4} atm.[31] The Arrhenius plot in figure 2 shows that the ionic transport is nearly pO_2 indipendent.

To clarify such effects in the condution mechanisms, several cycles were carried out both changing the temperature and tuning the pO_2 concentration in the enviroment. Particularly, figure 2-bottom show the Brower-like plots for the 40 and 80 nm samples N= 20, in Air, O_2, N_2 and several N_2-H_2 gas mixtures. The conductivity behaviour of the sample appears rather uncommon for pure ionic conductors such as YSZ and Bi_2O_3. A rapid change of conductivity is registered for all the sample from high pO_2 to low pO_2 at any temperatures at around 10^{-3} atm, depending on the temperatures. The change is particularly fast in the 40 nm sample, where several cycles (3) were carried out by increasing and decreasing the pO_2. In the cycling the samples showed reversibility of the changes. Moreover, the conductivity appeared rather constant at low pO_2, suggesting the presence of pure ionic conductivity under reducing conditions. Such a kind of electrical properties are not seen in YSZ and they can be attributed either to the Bi_2O_3 component or to the YSZ/Bi_2O_3 interfaces.

Further structural charcaterization was carried out by XRD by varying the pO_2 and using STEM-HAADF to check the strutural integrity of the sample after the electrochemical characterization (**Figure 3**). Both XRD peak *in-situ* characterization (figure 3 up) of the 40 nm sample indicated that the heterostruture preserves the crystallinity with a sligh change in the lattice size. Similar outcomes have been also reporterd in our previous work on pure and stabilitzed Bi_2O_3 in YSZ and CGO heterostrucuteres.[13] The atomic arrangement of the heterostructure is shown in the HAADF-STEM image in Figure 3 bottom, revealing structural coherency along the direction the growth. HAADF-STEM images and EDX compositional analysis of the heterostructure show integrity of the sample after the measument, in agreement with the XRD results.

We perform DFT calculations, to better explain, at the atomistic level, the role of vacancies and their concentration in the stability of Bi_2O_3 and ionic conductivity. Bi_2O_3 shows a variety of polymorphs, from the most stable α-phase (monoclinic), to the β- and δ-phases (tetragonal and cubic, which have an energy of around 20 and 70 meV above the one of the α-phase [32]). As the energy difference between these polimorphic structures is rather low, a change in the external conditions during the synthesis, such as pO_2, strain or nanoconfinement, could be enough to favour one higher energetic polymorph with respect to the ground state one. **Figure 4**, shows the energy difference between the δ- and α-phases as a function of the concentration of the oxygen vacancies. Although at a low concentration of vacancies, the α-phase is more favourable, increasing the concentration of vacancies, the metastable δ-phase becomes the thermodynamically most stable phase. Because of the nanoconfinement between the YSZ and Bi_2O_3 layers, the Bi_2O_3 phase stays trapped in its δ-phase also after the synthesis, at pO_2 which should, instead, favour the transition towards the α-phase.

To explain the change in the ionic conductivity as a function of pO_2, we calculate the diffusion barriers of oxygen vacancies in Bi_2O_3. To reduce the interaction between the neighboring vacancies, we now consider a supercell of δ-Bi_2O_3 built by repeating the unit cell of Bi_2O_3 2x2x2 times. It has been previously shown that the (110) vacancy alignment is the most favorable in δ-Bi_2O_3.[33] We have calculated the oxygen vacancy diffusion barriers in different vacancies configurations for one and two vacancies, as shown in **Figure 5**. While the diffusion barrier for one vacancy is of the order of 0.9 eV, the average value for diffusion barrier for two vacancies, which are close to each other is around 1.5 eV. Because of the preferred distribution, the energy barrier for diffusion increases together with the vacancy concentration. A possible explanation of the difference in the activation energy at high and low pO_2 can be related with the diffusion barriers in these two cases: the one vacancy configuration can well approximate the high pO_2 limit, and the two vacancies structure well correlates with the activation energy in the low pO_2 limit. This (bulk) model, however, does not consider the role of the interfaces, which can also have an effect in modifying the activation barriers.

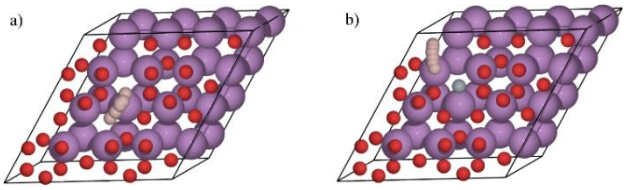

Figure 5: Example of NEB paths: the diffusion of the oxygen vacancy is indicated in pink for the (a) one- and (b) two-vacancy structures (in the latter, the position of the other vacancy is indicated in grey). Bi atoms are indicated in purple and oxygen atoms in red. The average diffusion barriers are 0.9 eV for the one-vacancy structures and 1.5 eV for the two-vacancy ones.

4. Conclusions

Cubic sesquioxide is stabilized in YSZ heterostrutures as thin film multilayers for a total thickness below 100 nm. The material show remarkably high electric conductivity and low

activation energy values in air that are superior to the materials components. At low pO_2 below 10^{-5} atm, the heterostructure has rather stable conductivity, although lower than in air. Such properties are not expected by mixing two of properties and they likely rise by nanostructuring Bi_2O_3 and exposing it to low pO_2 conditions. A possible explanation for the different activation energies at high and low pO2 has been provided using DFT results and it is connected with the energy barriers for vacancy diffusion being higher for high concentration of vacancies compared to a low vacancy concentration configuration.

Acknowledgements

This research was partially supported by the Danish Council for Independent Research Technology and Production Sciences for the DFF- Research Project 2 (Grant No. 48293).

References

[1] Wang G, Yang Y, Han D and Li Y 2017 Oxygen defective metal oxides for energy conversion and storage *Nano Today* **13** 23–39

[2] Kan W H, Samson A J and Thangadurai V 2016 Trends in electrode development for next generation solid oxide fuel cells *J. Mater. Chem. A* **4** 17913–32

[3] Swallow J G, Kim J J, Maloney J M, Chen D, Smith J F, Bishop S R, Tuller H L and Van Vliet K J 2017 Dynamic chemical expansion of thin-film non-stoichiometric oxides at extreme temperatures *Nat. Mater.* **16** 749–54

[4] Lee D, Park J-W, Cho N-K, Lee J and Kim Y S 2019 Verification of Charge Transfer in Metal-Insulator-Oxide Semiconductor Diodes via Defect Engineering of Insulator *Sci. Rep.* **9** 10323

[5] Tarnuzzer R W, Colon J, Patil S and Seal S 2005 Vacancy Engineered Ceria Nanostructures for Protection from Radiation-Induced Cellular Damage *Nano Lett.* **5** 2573–7

[6] Pryds N and Esposito V 2017 When two become one: An insight into 2D conductive oxide interfaces *J. Electroceramics* **38** 1–23

[7] Maier J 2005 Nanoionics: ion transport and electrochemical storage in confined systems *Nat. Mater.* **4** 805–15

[8] Yao L, Inkinen S and van Dijken S 2017 Direct observation of oxygen vacancy-driven structural and resistive phase transitions in La2/3Sr1/3MnO3 *Nat. Commun.* **8** 14544

[9] Li Y, Sanna S, Norrman K, Christensen D V, Pedersen C S, Lastra J M G, Traulsen M L, Esposito V and Pryds N 2019 Tuning the stoichiometry and electrical properties of tantalum oxide thin films *Appl. Surf. Sci.* **470** 1071–4

[10] Christensen D V., Chen Y, Esposito V and Pryds N 2019 The role of oxide interfaces in highly confined electronic and ionic conductors *APL Mater.* **7** 0–7

[11] Garbayo I, Chiabrera F, Alayo N, Santiso J, Morata A and Tarancón A 2019 Thin film oxide-ion conducting electrolyte for near room temperature applications *J. Mater. Chem. A* **7** 25772–8

[12] Perin G, Gadea C, Rosa M, Sanna S, Xu Y, Kiebach R, Glisenti A and Esposito V 2019 Gd0.2Ce0.8O1.9/Y0.16Zr0.84O1.92 nanocomposite thin films for low temperature ionic conductivity *J. Phys. Chem. Solids* **132** 162–71

[13] Sanna S, Esposito V, Andreasen J W, Hjelm J, Zhang W, Kasama T, Simonsen S B, Christensen M, Linderoth S and Pryds N 2015 Enhancement of the chemical stability in confined δ -Bi 2 O 3 *Nat. Mater.* **14** 500–4

[14] Jiang N and Wachsman E D 2004 Structural Stability and Conductivity of Phase-Stabilized Cubic Bismuth Oxides *J. Am. Ceram. Soc.* **82** 3057–64

[15] Wachsman E D and Lee K T 2011 Lowering the Temperature of Solid Oxide Fuel Cells *Science (80-.).* **334** 935–9

[16] Sanna S, Esposito V, Christensen M and Pryds N 2016 High ionic conductivity in confined bismuth oxide-based heterostructures *APL Mater.* **4** 121101

[17] Alberi K, Nardelli M B, Zakutayev A, Mitas L, Curtarolo S, Jain A, Fornari M, Marzari N, Takeuchi I, Green M L, Kanatzidis M, Toney M F, Butenko S, Meredig B, Lany S, Kattner U, Davydov A, Toberer E S, Stevanovic V, Walsh A, Park N G, Aspuru-Guzik A, Tabor D P, Nelson J, Murphy J, Setlur A, Gregoire J, Li H, Xiao R, Ludwig A, Martin L W, Rappe A M, Wei S H and Perkins J 2019 *The 2019 materials by design roadmap* vol 52

[18] Mortensen J J, Hansen L B and Jacobsen K W 2005 Real-space grid implementation of the projector augmented wave method *Phys. Rev. B* **71** 035109

[19] Enkovaara J, Rostgaard C, Mortensen J J, Chen J, Duľak M, Ferrighi L, Gavnholt J, Glinsvad C, Haikola V, Hansen H A, Kristoffersen H H, Kuisma M, Larsen A H, Lehtovaara L, Ljungberg M, Lopez-Acevedo O, Moses P G, Ojanen J, Olsen T, Petzold V, Romero N A, Stausholm-Møller J, Strange M, Tritsaris G A, Vanin M, Walter M, Hammer B, Häkkinen H, Madsen G K H, Nieminen R M, Nørskov J K, Puska M, Rantala T T, Schiøtz J, Thygesen K S and Jacobsen K W 2010 Electronic structure calculations with GPAW: a real-space implementation of the projector augmented-wave method *J. Phys. Condens. Matter* **22** 253202

[20] Larsen A H, Mortensen J J, Blomqvist J, \bf I. E. Castelli, Christensen R, Duľak M, Friis J, Groves M N, Hammer B, Hargus C, Hermes E D, Jennings P C, Jensen P B, Kermode J, Kitchin J R, Kolsbjerg E L, Kubal J, Kaasbjerg K, Lysgaard S, Maronsson J B, Maxson T, Olsen T, Pastewka L, Peterson A, Rostgaard C, Schiøtz J, Schütt O, Strange M, Thygesen K S, Vegge T, Vilhelmsen L, Walter M, Zeng Z and Jacobsen K W 2017 The atomic simulation environment{\textemdash}a Python library for working with atoms *J. Phys. Condens. Matter* **29** 273002

[21] Perdew J P, Ruzsinszky A, Csonka G I, Vydrov O A, Scuseria G E, Constantin L A, Zhou X and Burke K 2008 Restoring the Density-Gradient Expansion for Exchange in Solids and Surfaces *Phys. Rev. Lett.* **100** 136406

[22] Henkelman G and Jónsson H 2000 Improved tangent estimate in the nudged elastic band method for finding minimum energy paths and saddle points *J. Chem. Phys.* **113** 9978–85

[23] Kolsbjerg E L, Groves M N and Hammer B 2016 An automated nudged elastic band method *J. Chem. Phys.* **145** 094107

[24] Sanna S, Esposito V, Pergolesi D, Orsini A, Tebano A, Licoccia S, Balestrino G and Traversa E 2009 Fabrication and electrochemical properties of epitaxial samarium-doped ceria films on SrTiO3-buffered MgO substrates *Adv. Funct. Mater.* **19** 1713–9

[25] Sanna S, Esposito V, Tebano A, Licoccia S, Traversa E and Balestrino G 2010 Enhancement of Ionic Conductivity in Sm-Doped Ceria/Yttria-Stabilized Zirconia Heteroepitaxial Structures *Small* **6** 1863–7

[26] Dos Santos-Gómez L, Sanna S, Norby P, Pryds N, Losilla E R, Marrero-López D and Esposito V 2019 Electrochemical stability of (La,Sr)CoO 3-δ in (La,Sr)CoO 3-δ /(Ce, Gd)O 2-delta; Heterostructures *Nanoscale* **11** 2916–24

[27] Sanna S, Esposito V, Graves C, Hjelm J, Andreasen J W and Pryds N 2014 Structural instability and electrical properties in epitaxial Er 2O3-stabilized Bi2O3 thin films *Solid State Ionics* **266** 13–8

[28] Gomez C L, Depablos-Rivera O, Medina J C, Silva-Bermudez P, Muhl S, Zeinert A and Rodil S E 2014 Stabilization of the delta-phase in Bi 2 O 3 thin films *Solid State Ionics* **255** 147–52

[29] Orlova E I, Kharitonova E P, Gorshkov N V, Goffman V G and Voronkova V I 2017 Phase formation and electrical properties of Bi 2 O 3 -based compounds in the Bi 2 O 3 -La 2 O 3 -MoO 3 system *Solid State Ionics* **302** 158–64

[30] Raza M, Sanna S, Dos Santos Gómez L, Gautron E, El Mel A A, Pryds N, Snyders R, Konstantinidis S and Esposito V 2018 Near interface ionic transport in oxygen vacancy stabilized cubic zirconium oxide thin films *Phys. Chem. Chem. Phys.* **20** 26068–71

[31] Takahashi T, Esaka T and Iwahara H 1977

Conduction in Bi2O3-based oxide ion conductors under low oxygen pressure. I. Current blackening of the Bi2O3-Y2O3 electrolyte *J. Appl. Electrochem.* **7** 299–302

[32] Sun W, Dacek S T, Ong S P, Hautier G, Jain A, Richards W D, Gamst A C, Persson K A and Ceder G 2016 The thermodynamic scale of inorganic crystalline metastability *Sci. Adv.* **2** e1600225

[33] Zhong G, Wang Y, Dai Z, Wang J and Zeng Z 2009 Oxygen vacancy configuration of δ-Bi 2 O 3 : an ab initio study *Phys. status solidi* **246** 97–101